


# Transverse Magnetic Mode Laser in Photonic Crystal Nanobeam Cavity

Taesu Ryu,<sup>1</sup> Hwi-Min Kim,<sup>2</sup> Sang-Woo Ki,<sup>1</sup> Yong-Hee Lee,<sup>2</sup> and Jin-Kyu Yang<sup>1,3,\*</sup>

<sup>1</sup>*Department of Optical Engineering, Kongju National University, Cheonan 31080, Republic of Korea*

<sup>2</sup>*Department of Physics, Korea Advanced Institute of Science and Technology (KAIST), Daejeon 34141, Republic of Korea*

<sup>3</sup>*Institute of Application and Fusion for Light, Kongju National University, Cheonan 31080, Republic of Korea*

 (Received 22 December 2022; revised 4 March 2023; accepted 21 April 2023; published 16 May 2023)

We experimentally demonstrate a transverse magnetic (TM) mode laser in a photonic crystal (PhC) slab structure at room temperature. This study proposes a PhC nanobeam (NB) cavity to support a high-quality-factor ( $Q$ -factor) TM mode. For a large and complete photonic band gap, the PhC NB structures consist of large air holes in a thick dielectric slab. The PhC NB cavity is optimized numerically for a high- $Q$ -factor TM mode of over 1 000 000 by reducing the radii of the air holes quadratically from the center to the edge of the PhC NB. A single-TM-mode lasing action is observed in an In-Ga-As-P quantum well (QW)-embedded optimized PhC NB cavity structure at room temperature via optical pulse pumping, where the QW layer is lightly etched. We believe that the TM mode lasers in PhC NB cavities with a lightly etched QW can be good candidates for a surface plasmon excitation source or a highly sensitive optical sensor.

DOI: [10.1103/PhysRevApplied.19.054053](https://doi.org/10.1103/PhysRevApplied.19.054053)

## I. INTRODUCTION

Photonic crystals (PhCs) are employed to control the light-matter interaction using the photonic band gap (PBG) effect [1–3]. In particular, two-dimensional (2D) PhC slab structures have been considered a useful platform for photonic integrated circuits owing to the three-dimensional (3D) perfect guiding [4,5], easy fabrication [6,7], and scalability of such structures [8]. However, most of the studies conducted on the topic have been related to the transverse electric (TE) mode because of the existence of large PBG for TE polarization and weak coupling between TE and transverse magnetic (TM) polarizations in a thin slab [9]. Since Notomi's report, a nanobeam (NB) structure has been substituted for a 2D PhC slab structure owing to not only the ultrahigh quality ( $Q$ ) factor but also the smallest possible dielectric cavity [10–12]. There are several advantages of the NB cavity: for example, the simple structure for a high- $Q$ -factor cavity [11,12], low laser threshold [13–15], high-density integration [16,17], ultralow-power optical switching [18,19], and easy integration with a silicon waveguide geometry [20]. Hence, various sensor applications of NB cavities have been demonstrated, such as refractive index sensing [21–23], nanoprobe for biosensing [24], optomechanical sensing [25], and magnetic field sensing [26]. It was reported that thick NB structures can have high- $Q$ -factor resonant modes with

both TE and TM polarizations [27]. In our previous report, we proposed that a thick NB cavity with a horizon air gap can be a good candidate for ultrasensitive refractive index sensing [23]. However, there has been no experimental demonstration of TM-mode lasers in NB slab structures because of the discouragement of the coupling to the TM mode in compressive strain at quantum wells (QWs) [28]. There are properties peculiar to TM polarization, such as surface plasmon excitation and strong confinement in the horizontal air gap. In this study, we propose a NB cavity with a thick slab that consists of a 1D array of air holes with quadratic size modification. The numerical results show that a NB structure with a thick slab has a large and complete PBG. In addition, we experimentally demonstrate a single-TM-mode laser operation in an optimized NB cavity with an In-Ga-As-P multiple QW layer, which is lightly etched for sensing applications. The lasing mode is confirmed by numerical simulation based on a scanning electron microscopy (SEM) image of the sample. We believe that the TM-mode NB laser is a good candidate for a compact on-chip TM-polarization light source for surface plasmon excitation and has various sensor applications.

## II. DESIGN AND OPTIMIZATION

The photonic band structures of NBs are calculated using the plane wave expansion method with MPB (MIT Photonic Bands) simulation software [29,30]. The structural parameters are indicated in the right-hand inset of Fig. 1(a). The period ( $a$ ), thickness ( $t$ ), width ( $w$ ), and

\*jinkyuyang@kongju.ac.kr

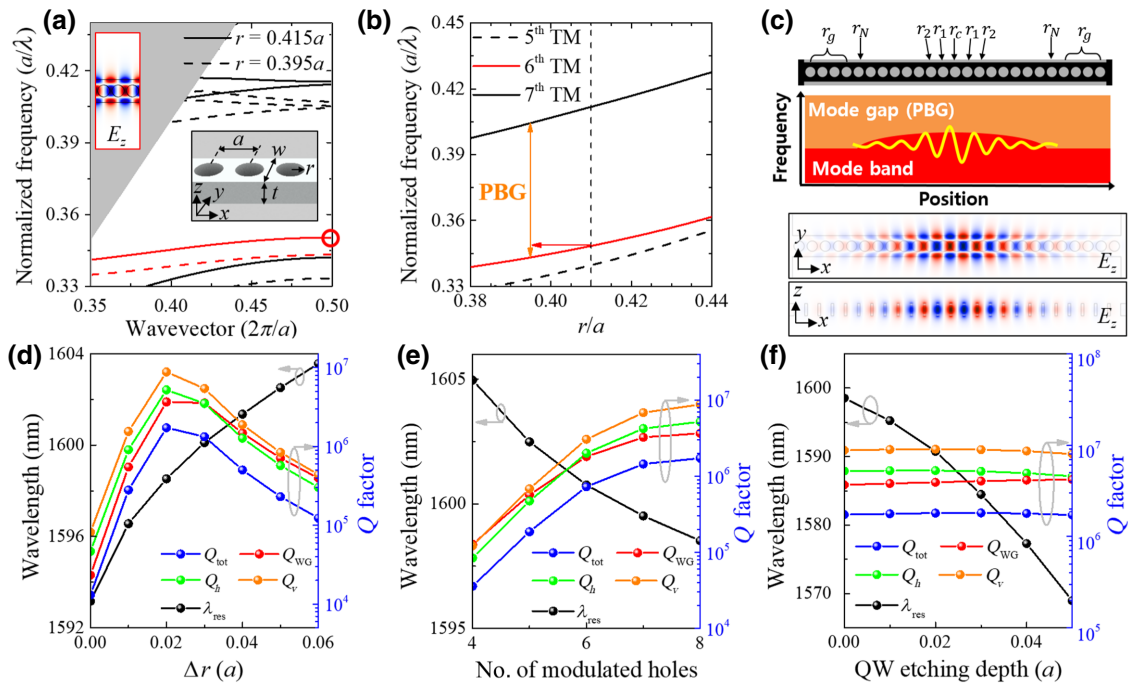


FIG. 1. Optimization of NB cavity. (a) Photonic band structure of NB with  $r/a = 0.415$  (solid lines) and  $r/a = 0.395$  (dashed lines). (b) Normalized frequency of the TM BE mode ( $k = \pi/a$ ) as a function of the radius of the air hole. (c)  $E_z$  field profile of TM cavity mode at the horizontal plane (upper) and vertical plane (lower). Wavelength and  $Q$  factor of TM cavity mode as a function of (d) maximum difference of radii, (e) number of modulated holes, and (f) QW etching depth. The left-hand inset in (a) indicates the  $E_z$  field profile of the sixth TM BE mode marked with the red circle and the right-hand inset in (a) is a schematic image of the NB structure. The upper insets in (c) show the cut-view of the NB cavity and the strategy of light confinement in the cavity by reducing air holes quadratically.

refractive index of the slab are set as 563 nm, 520 nm, 1.6*a*, and 3.25, respectively. Figure 1(a) shows the band structures for two different hole sizes ( $r/a = 0.415$  and 0.395). For each case, a wide PBG is observed between the sixth TM band (red solid line) and the seventh TM band (black solid line). The normal electric field ( $E_z$ ) profile of the sixth TM band-edge (BE) mode at the wavevector,  $k = \pi/a$  (red circle), is shown in the inset of Fig. 1(a). Subsequently, we obtain the frequency of the TM BE mode as a function of the radius. As shown in Fig. 1(b), as the radius increases, the TM bands blue-shift owing to the reduction in dielectric materials. Therefore, if a NB with a large air hole is surrounded by a NB with small air holes, the sixth TM BE mode can be localized in the region of large air holes owing to the PBG effect of the NB with small air holes. Moreover, the sixth TM BE mode lies inside the TE pseudo-band-gap; therefore, the sixth TM BE mode can be strongly confined by a complete PBG effect [31]. The TM cavity mode of the NBs is optimized using the home-made 3D finite-difference time-domain (FDTD) method. The NB cavity in Fig. 1(c) is composed of 25 air holes, which are gradually tapered according to the following equation [23]:

$$r_i = r_c - \Delta r \times i^2/N^2, \quad (1)$$

where  $r_i$  is the radius of the  $i$ th air hole,  $r_c$  is the radius of the center air hole,  $\Delta r$  is the maximum difference between the air hole radii in the NB,  $N$  is the number of modulated air holes on one side, and  $i$  is the index of the air hole position from the center. To minimize propagation loss along the waveguide, we set the radius of the air holes surrounding the modulated holes equal to  $r_N$  (i.e.,  $r_g = r_N$ ). Figure 1(c) shows  $xy$ - and  $xz$ -cut views of the  $E_z$  field profile of the optimized TM cavity mode. The amplitude of the  $E_z$  field has a maximum at the center and gradually decreases along the NB.

First, we investigate the effect of  $\Delta r$  on the  $Q$  factor ( $Q_{\text{tot}}$ ) at fixed  $N$ . The total cavity loss ( $1/Q_{\text{tot}}$ ) is decomposed into waveguide propagation loss ( $1/Q_{\text{WG}}$ ), vertical scattering loss ( $1/Q_v$ ), and horizontal scattering loss ( $1/Q_h$ ). For  $N = 8$ , the  $Q$  factor is maximized at approximately 2 000 000 when  $\Delta r$  is set to  $0.02a$ , owing to the minimum optical loss in all channels, as shown in Fig. 1(d). Subsequently, we set  $\Delta r$  to  $0.02a$  and calculate the  $Q$  factor as a function of  $N$ , as shown in Fig. 1(e). The  $Q$  factor increases and saturates as  $N$  increases, owing to the saturation of the cavity loss in all channels. We also investigate the  $Q$  factor and resonant wavelength as functions of the QW etching depth. The  $Q$  factor remains unchanged but the wavelength shifts significantly. This implies that

the electric field intensity is strongly localized in the QW etching region, which is advantageous for highly sensitive optical sensing [32,33].

### III. FABRICATION

Optimized NB cavities are prepared using a standard fabrication technique for III-V semiconductor nanolasers [34,35]. In this study, we fabricate NB cavities on two types of In-Ga-As-P QW wafers. One is an In-P/In-Ga-As-P QW slab on an In-Ga-As sacrificial layer and the other is an In-Ga-As-P/In-Ga-As-P QW slab on an In-P sacrificial layer. We name the NB cavities fabricated on the In-P/In-Ga-As-P QW wafer and In-Ga-As-P/In-Ga-As-P QW wafer as In-P NBs and In-Ga-As-P NBs, respectively. The fabrication process is identical for both wafers, except for the final wet-etching step [36]. First, poly(methyl methacrylate) (PMMA) is spin-coated onto the wafer. Next, photonic crystal patterns are defined using electron-beam lithography. The PMMA layer is hardened by electron-beam irradiation and Ar ion milling, and the pattern is transferred to wafers by chemically assisted ion-beam etching. The PMMA layer is removed by O<sub>2</sub> plasma ashing. Finally, for the In-P NBs, the membrane is subsequently released by two etching processes. The first wet-etching process involves removing the In-Ga-As sacrificial layer underneath the In-P slab using a mixture of succinic acid solution (C<sub>4</sub>H<sub>6</sub>O<sub>4</sub>) and hydrogen peroxide (H<sub>2</sub>O<sub>2</sub>) in a volume ratio of 20:1 at room temperature. A second wet etching is performed to selectively remove the In-Ga-As-P QW layer with a mixture of citric acid solution (C<sub>6</sub>H<sub>8</sub>O<sub>7</sub>) and hydrogen peroxide in a volume ratio of 5:1 at a low temperature of approximately 4 °C [37,38]. From the SEM images in Fig. 2(a), the thickness of the In-P is estimated to be approximately 520 nm, and the QW etching depth is approximately 17 nm. It is worth noting that the QW layer is atomically flat owing to the epitaxial growth, so the thickness of the etched QW is also ultrauniform, which can enhance the sensitivity of the refractive index of the surrounding media by monitoring the frequency of the

TM mode [23,32,37]. For the In-Ga-As-P NBs, a single wet-etching process is performed with 20% diluted HCl solution to remove the In-P sacrificial layer. The thickness of the In-Ga-As-P slab is approximately 530 nm, as shown in Fig. 2(b). During the wet-etching process, there is no issue about stiction because the slab thickness is about two times thicker than a typical nanobeam cavity for TE modes [11,13,14,35].

### IV. CHARACTERIZATION AND DISCUSSION

We optically characterize the fabricated devices with a 980-nm laser diode at room temperature, where the pulse duration and width are 2 μs and 10 ns, respectively. The pump beam is focused on the device via an objective lens at 40× magnification. The pump spot size is estimated as 3 μm in diameter. Photoluminescence (PL) is collected with the same objective lens and delivered to the monochromator to analyze the spectral characteristics of the lasing mode [39].

We observe single-mode operation from both In-P NBs and In-Ga-As-P NBs. Figure 3 shows the lasing spectra of the two In-P NBs at room temperature. Single-lasing peaks are observed at 1534 and 1594 nm. From the SEM image, the structural parameters are estimated to be:  $a = 563$  nm,  $r_c = 0.415a$ ,  $r_g = 0.399a$ , and  $w = 1.60a$ . In order to figure out what the lasing mode comes from, we perform 3D FDTD simulation with the estimated structural values from the SEM image of the lasing sample to compare the resonant wavelength of the high- $Q$  mode with the peak wavelength in the emission spectra. One TM mode with a high  $Q$  factor is found near a lasing wavelength of 1534 nm. The calculated wavelength and  $Q$  factor are 1555 nm and 160 000, respectively. In addition, the  $E_z$  field profile is identical to that of the target TM BE mode, as shown in the inset of Fig. 3(a). In particular, the electric field intensity is strongly localized at the boundary of the NB, where the QW is lightly etched laterally [23,40]. There is also a TE cavity mode [41]. However, the calculated wavelength is 1508 nm, which is far from the lasing peak, and the  $Q$  factor is 1000, which is less favorable for lasing

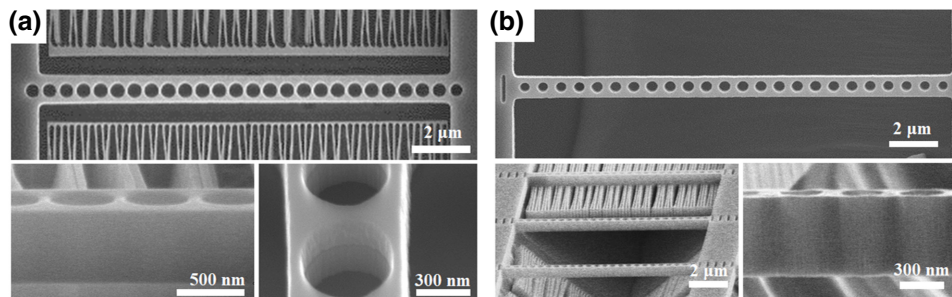


FIG. 2. SEM images of the fabricated In-Ga-As-P QW-embedded NB cavity samples. (a) In-P NB slab sample. (b) In-Ga-As-P NB slab sample.

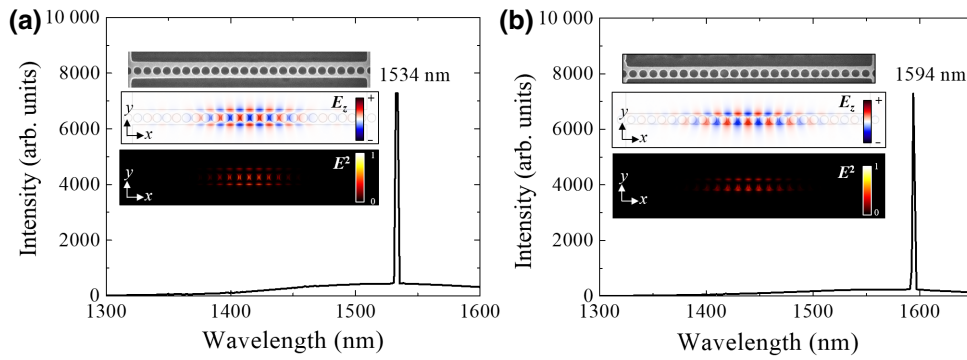


FIG. 3. Lasing spectra from the In-P NB samples. (a) Lasing spectrum from the TM mode in the symmetric NB sample. (b) Lasing spectrum from the TM mode in the asymmetric NB sample. The inset images are the sample SEM image, the calculated  $E_z$  field, and  $E^2$  profile of the TM mode from top to bottom, respectively.

action. We perform the same analysis on the asymmetrical In-P NB laser, as shown in the top inset of Fig. 3(b). The estimated structural parameters are as follows:  $a = 571$  nm,  $r_c = 0.407a$ ,  $r_g = 0.349a$ , and  $w = 1.10a$ . We find a TM mode with a wavelength of 1618 nm and a  $Q$  factor of 17 000, as shown in the middle inset of Fig. 3(b). There is a TE mode at a wavelength of 1441 nm, but the  $Q$  factor is 520 [41]. Owing to the inherent radiation characteristics of the TM mode, the emission is not captured with an infrared charged-coupled device. In addition, because of the poor thermal conductivity of the QW etching NB cavity, we cannot obtain the light-in-light-out (LL) curve and near-field image at the lasing action.

In addition, we observe the lasing action of the TE mode from In-Ga-As-P NBs. From the SEM image in the top inset of Fig. 4(a), the structural parameters are estimated as follows:  $a = 573$  nm,  $r_c = 0.343a$ ,  $r_g = 0.302a$ , and  $w = 1.12a$ . Here, the thickness of the In-Ga-As-P slab is 530 nm, which is 10 nm thicker than that of the In-P slab. With 3D FDTD simulation, a TE mode is found near the lasing wavelength of 1473 nm. The simulated wavelength

is 1478 nm and the  $Q$  factor is approximately 150 000 [31]. There is a TM mode at a wavelength of 1447 nm, but the  $Q$  factor is relatively low at approximately 44 000. In particular, the  $H_z$  field profile of the TE mode is well balanced to reduce the optical loss similar to the photonic bound states in the continuum [42]. Figure 4(b) shows the LL and linewidth characteristics that have threshold behavior of lasing action. The threshold peak pump power is 160  $\mu$ W and linewidth reduction is observed near the threshold. It is worth noting that the corresponding threshold power density of about 2.3 kW/cm<sup>2</sup> is a typical value in PhC NB lasers [14,15,37], and the slit in experiments is set to 100  $\mu$ m, which corresponds to 1-nm spectral resolution [43]. The near-field image shown in the inset of Fig. 4(b) is captured above threshold, which reveals a strong spot at the center of the NB marked with the white dashed line. It is evidence that the lasing mode is strongly localized in the NB. Figure 4(c) shows typical lasing characteristics of evolution of the emission spectrum with increasing pump power, where one peak grows rapidly with increasing pump power. The laser emission is linearly polarized

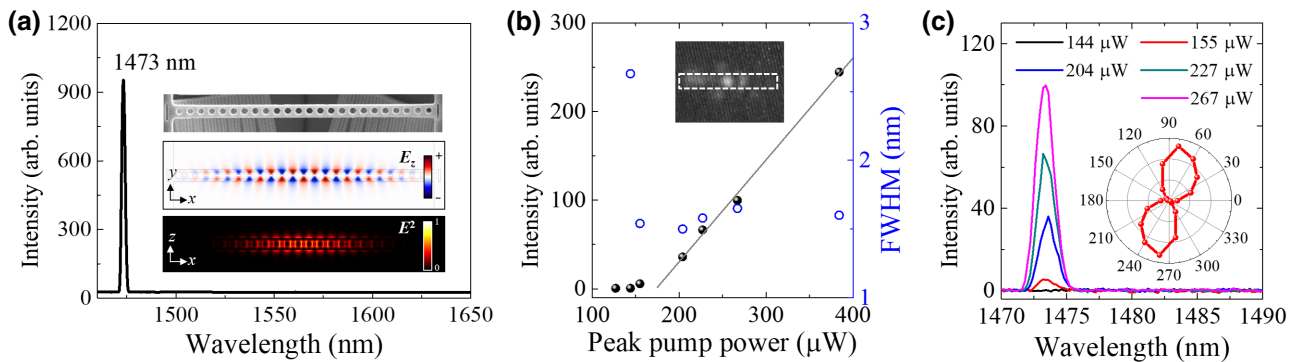


FIG. 4. Characteristics of lasing action from the In-Ga-As-P NB sample. (a) Lasing spectrum from the NB sample. (b) LL curve. (c) PL spectra at different pump powers. The inset images in (a) are the sample SEM image, the calculated  $H_z$  field profile of the TE cavity mode in the normal direction, and the  $E^2$  profile from top to bottom, respectively. The insets in (b),(c) are the near-field image and the polarization property at lasing action, respectively.

along the perpendicular to the length of the NB as shown in the inset in Fig. 4(c), which is one typical property of a NB laser [13–15,35]. From the polarization state and the near-field image of a laser, we can see whether the lasing mode is coming from the TE mode or the TM mode [44]. In the case of TE mode, the radiation direction is essentially perpendicular to the slab, so a sharp spot image and linear polarization perpendicular to the NB direction are observed above threshold. However, in case of TM mode, the radiation direction is parallel to the slab, so the near-field image is not clear and the polarization is not perfectly linear. We characterize multiple In-Ga-As-P NBs and observe lasing actions primarily from TE cavity modes [44]. Multimode lasing originates from the third TE mode, and the sixth TM cavity mode is also observed, which is confirmed by 3D FDTD analysis with estimated parameters [44,45]. It is worth noting that due to the inaccuracy of the refractive index of the In-Ga-As-P/In-P slab and the error of the extracted structural parameters, there may be some error between the lasing peak wavelength and the calculated resonant wavelength.

## V. CONCLUSION

We experimentally demonstrate TM-mode lasers in a thick PhC NB slab structure at room temperature. The NB cavity is numerically optimized by gradually reducing the air holes from the center to the edge of the NB cavity to realize a high- $Q$  TM mode of over 1 000 000. Two types of TM-mode lasers are fabricated on two epitaxial wafers. The first type is In-P NBs, in which a QW is laterally etched to enhance environmental sensitivity, and the second type is In-Ga-As-P NBs without QW etching. Single-mode lasing action is observed in both In-P NB and In-Ga-As-P NB at room temperature via optical pulse pumping. The TM laser mode is confirmed by SEM image-based numerical simulations. We believe that TM-mode lasers with a lightly etched QW can be an efficient surface plasmon polariton excitation source and be used as highly sensitive optical sensors.

## ACKNOWLEDGMENTS

This work was supported by the Basic Science Research Program through the National Research Foundation of Korea (NRF) funded by the Ministry of Science and ICT (No. 2020R1A2C1014498) and a research grant from Kongju National University in 2020.

[1] E. Yablonovitch, Inhibited Spontaneous Emission in Solid-State Physics and Electronics, *Phys. Rev. Lett.* **58**, 2059 (1987).

- [2] S. John, Strong Localization of Photons in Certain Disordered Dielectric Superlattices, *Phys. Rev. Lett.* **58**, 2486 (1987).
- [3] S. Noda, M. Fujita, and T. Asano, Spontaneous-emission control by photonic crystals and nanocavities, *Nat. Photon.* **1**, 449 (2007).
- [4] A. Chutinan and S. Noda, Highly confined waveguides and waveguide bends in three-dimensional photonic crystal, *Appl. Phys. Lett.* **75**, 3739 (1999).
- [5] W. Lee, S. A. Pruzinsky, and P. V. Braun, Multi-photon polymerization of waveguide structures within three-dimensional photonic crystals, *Adv. Mater.* **14**, 271 (2002).
- [6] C. M. Soukoulis, The history and a review of the modelling and fabrication of photonic crystals, *Nanotechnology* **13**, 420 (2002).
- [7] J. Hou, M. Li, and Y. Song, Patterned colloidal photonic crystals, *Angew. Chem. Int. Ed.* **130**, 2571 (2018).
- [8] J. D. Joannopoulos, P. R. Villeneuve, and S. Fan, Photonic crystals: Putting a new twist on light, *Nature* **386**, 143 (1997).
- [9] S. G. Johnson, S. Fan, P. R. Villeneuve, J. D. Joannopoulos, and L. A. Kolodziejski, Guided modes in photonic crystal slabs, *Phys. Rev. B* **60**, 5751 (1999).
- [10] M. Notomi, E. Kuramochi, and H. Taniyama, Ultrahigh- $Q$  nanocavity with 1D photonic gap, *Opt. Express* **16**, 11095 (2008).
- [11] P. B. Deotare, M. W. McCutcheon, I. W. Frank, M. Khan, and M. Lončar, High quality factor photonic crystal nanobeam cavities, *Appl. Phys. Lett.* **94**, 121106 (2009).
- [12] D. Yang, P. Zhang, H. Tian, Y. Ji, and Q. Quan, Silicon on-chip one-dimensional photonic crystal nanobeam bandgap filter integrated with nanobeam cavity for accurate refractive index sensing, *IEEE Photonics J.* **7**, 1 (2015).
- [13] S. Kim, B.-H. Ahn, J.-Y. Kim, K.-Y. Jeong, K. S. Kim, and Y.-H. Lee, Nanobeam photonic bandedge lasers, *Opt. Express* **19**, 24055 (2011).
- [14] K.-Y. Jeong, Y. Hwang, K. S. Kim, M.-K. Seo, H.-G. Park, and Y.-H. Lee, Electrically driven nanobeam laser, *Nat. Commun.* **4**, 2822 (2013).
- [15] Y. Zhang, M. Khan, Y. Huang, J. Ryou, P. Deotare, R. Dupuis, and M. Lončar, Photonic crystal nanobeam lasers, *Appl. Phys. Lett.* **97**, 051104 (2010).
- [16] P. B. Deotare, L. C. Kogos, I. Bulu, and M. Lončar, Photonic crystal nanobeam cavities for tunable filter and router applications, *IEEE J. Sel. Top. Quantum Electron.* **19**, 3600210 (2013).
- [17] D. Yang, X. Liu, X. Li, B. Duan, A. Wang, and Y. Xiao, Photonic crystal nanobeam cavity devices for on-chip integrated silicon photonics, *J. Semicond.* **42**, 023103 (2021).
- [18] A. Shakoor, K. Nozaki, E. Kuramochi, K. Nishiguchi, A. Shinya, and M. Notomi, Compact 1D-silicon photonic crystal electro-optic modulator operating with ultra-low switching voltage and energy, *Opt. Express* **22**, 28623 (2014).
- [19] P. Dong, L. Zhang, D. Dai, and Y. Shi, All-optical switching of silicon nanobeam cavities with an ultra-compact heater utilizing the photothermal effect, *ACS Photonics* **9**, 197 (2022).
- [20] J. Lee, I. Karnadi, J. T. Kim, Y.-H. Lee, and M.-K. Kim, Printed nanolaser on silicon, *ACS Photonics* **4**, 2117 (2017).

- [21] B. Wang, M. A. Dündar, R. Nötzel, F. Karouta, S. He, and R. W. van der Heijden, Photonic crystal slot nanobeam slow light waveguides for refractive index sensing, *Appl. Phys. Lett.* **97**, 151105 (2010).
- [22] Q. Qiao, J. Xia, C. Lee, and G. Zhou, Applications of photonic crystal nanobeam cavities for sensing, *Micromachines* **9**, 541 (2018).
- [23] J.-K. Yang, C.-Y. Kim, and M. Lee, High-sensitive TM modes in photonic crystal nanobeam cavity with horizontal air gap for refractive index sensing, *Appl. Sci.* **9**, 967 (2019).
- [24] G. Shambat, S. R. Kothapalli, J. Provine, T. Sarmiento, J. Harris, S. S. Gambhir, and J. Vučković, Single-cell photonic nanocavity probes, *Nano Lett.* **13**, 4999 (2013).
- [25] M. Wu, A. C. Hryciw, C. Healey, D. P. Lake, H. Jayakumar, M. R. Freeman, J. P. Davis, and P. E. Barclay, Dissipative and dispersive optomechanics in a nanocavity torque sensor, *Phys. Rev. X* **4**, 021052 (2014).
- [26] H. Du, G. Zhou, Y. Zhao, G. Chen, and F. S. Chau, Magnetic field sensor based on coupled photonic crystal nanobeam cavities, *Appl. Phys. Lett.* **110**, 061110 (2017).
- [27] M. W. McCutcheon, P. B. Deotare, Y. Zhang, and M. Lončar, High-Q transverse-electric/transverse-magnetic photonic crystal nanobeam cavities, *Appl. Phys. Lett.* **98**, 111117 (2011).
- [28] J. K. Hwang, H. Y. Ryu, D. S. Song, I. Y. Han, H. K. Park, D. H. Jang, and Y. H. Lee, Continuous room-temperature operation of optically pumped two-dimensional photonic crystal lasers at  $1.6\mu\text{m}$ , *IEEE Photonics Technol. Lett.* **12**, 1295 (2000).
- [29] J. D. Joannopoulos, S. G. Johnson, J. N. Winn, and R. D. Meade, *Molding the Flow of Light* (Princeton University Press, Princeton, NJ, 2008).
- [30] S. G. Johnson and J. D. Joannopoulos, Block-iterative frequency-domain methods for Maxwell's equations in a planewave basis, *Opt. Express* **8**, 173 (2001).
- [31] See Supplemental Material at <http://link.aps.org/supplemental/10.1103/PhysRevApplied.19.054053> for details of numerical results of photonic band structures of various NB structures.
- [32] S. Lee, S. C. Eom, J. S. Chang, C. Huh, G. Y. Sung, and J. H. Shin, Label-free optical biosensing using a horizontal air-slot  $\text{SiN}_x$  microdisk resonator, *Opt. Express* **18**, 20638 (2011).
- [33] T. W. Lu, P. T. Lin, and P. T. Lee, Photonic crystal horizontally slotted nanobeam cavity for silicon-based nanolasers, *Opt. Lett.* **37**, 569 (2012).
- [34] H.-G. Park, S.-H. Kim, S.-H. Kwon, Y.-G. Ju, J.-K. Yang, J.-H. Baek, S.-B. Kim, and Y.-H. Lee, Electrically driven single-cell photonic crystal laser, *Science* **305**, 1444 (2004).
- [35] S.-K. Moon, K.-Y. Jeong, H. Noh, and J.-K. Yang, Lasing in an optimized deterministic aperiodic nanobeam cavity, *Appl. Phys. Lett.* **109**, 241106 (2016).
- [36] See Supplemental Material at <http://link.aps.org/supplemental/10.1103/PhysRevApplied.19.054053> for fabrication procedures of NB cavity in In-P slab with QW etching and NB cavity in In-Ga-As-P slab without QW etching.
- [37] H. Jang, I. Karnadi, P. Pramudita, J.-H. Song, K. S. Kim, and Y.-H. Lee, Sub-microWatt threshold nanoisland lasers, *Nat. Commun.* **6**, 8276 (2015).
- [38] P. Pramudita, H. Jang, I. Karnadi, H.-M. Kim, and Y.-H. Lee, Self-aligned nanoislands nanobeam bandedge lasers, *Opt. Express* **25**, 6311 (2017).
- [39] See Supplemental Material at <http://link.aps.org/supplemental/10.1103/PhysRevApplied.19.054053> for details of experimental setup.
- [40] S. Lee, S. C. Eom, J. C. Chang, C. Huh, G. Y. Sung, and J. H. Shin, A silicon nitride microdisk resonator with a 40-nm-thin horizontal air slot, *Opt. Express* **18**, 11209 (2010).
- [41] See Supplemental Material at <http://link.aps.org/supplemental/10.1103/PhysRevApplied.19.054053> for details of numerical results of TE resonant modes in the In-P NB cavities using the estimated parameters.
- [42] X. Gao, C. W. Hsu, B. Zhen, X. Lin, J. D. Joannopoulos, M. Soljačić, and H. Chen, Formation mechanism of guided resonances and bound states in the continuum in photonic crystal slabs, *Sci. Rep.* **6**, 31908 (2016).
- [43] See Supplemental Material at <http://link.aps.org/supplemental/10.1103/PhysRevApplied.19.054053> for details of characteristics of lasing action in a PhC NB sample at different widths of entrance slit in monochromator.
- [44] See Supplemental Material at <http://link.aps.org/supplemental/10.1103/PhysRevApplied.19.054053> for details of characteristics of lasing action in various PhC NB samples in comparison with numerical results.
- [45] See Supplemental Material at <http://link.aps.org/supplemental/10.1103/PhysRevApplied.19.054053> for structural parameters of the samples, lasing peaks, and calculated results using the estimated structural parameters.